

# Thermally Aged Li–Mn–O Cathode with Stabilized Hybrid Cation and Anion Redox

Sa Li,\* Xin Sun, Yang Liu, Guang Liu, Weijiang Xue, Iradwikanari Waluyo, Zhi Zhu, Yunguang Zhu, Yanhao Dong,\* Yunhui Huang, and Ju Li\*

Cite This: *Nano Lett.* 2021, 21, 4176–4184

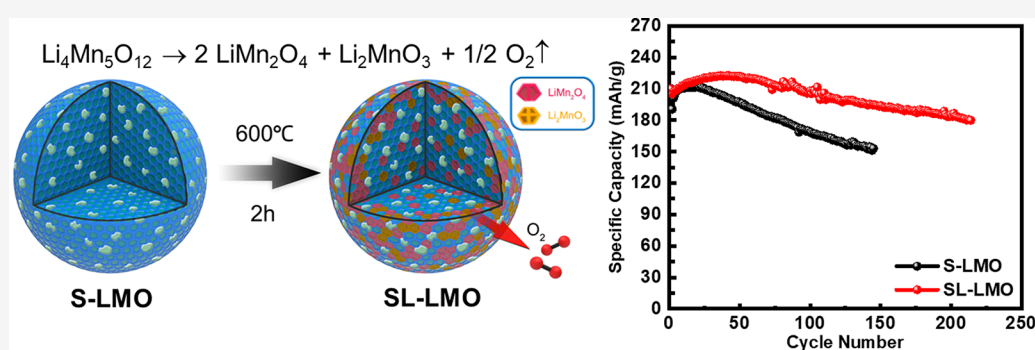
Read Online

ACCESS |

Metrics & More

Article Recommendations

Supporting Information



**ABSTRACT:** Though low-cost and environmentally friendly, Li–Mn–O cathodes suffer from low energy density. Although synthesized  $\text{Li}_4\text{Mn}_5\text{O}_{12}$ -like overlithiated spinel cathode with reversible hybrid anion- and cation-redox (HACR) activities has a high initial capacity, it degrades rapidly due to oxygen loss and side-reaction-induced electrolyte decomposition. Herein, we develop a two-step heat treatment to promote local decomposition as  $\text{Li}_4\text{Mn}_5\text{O}_{12} \rightarrow 2\text{LiMn}_2\text{O}_4 + \text{Li}_2\text{MnO}_3 + 1/2 \text{O}_2 \uparrow$ , which releases near-surface reactive oxygen that is harmful to cycling stability. The produced nanocomposite delivers a high discharge capacity of 225 mAh/g and energy density of over 700 Wh/kg at active-material level at a current density of 100 mA/g between 1.8 to 4.7 V. Benefiting from suppressed oxygen loss and side reactions, 80% capacity retention is achieved after 214 cycles in half cells. With industrially acceptable electrolyte amount (6 g/Ah), full cells paired with  $\text{Li}_4\text{Ti}_5\text{O}_{12}$  anode have a good retention over 100 cycles.

**KEYWORDS:**  $\text{Li}_4\text{Mn}_5\text{O}_{12}$ – $\text{LiMn}_2\text{O}_4$ – $\text{Li}_2\text{MnO}_3$  nanocomposite, Spinel/layered Li-rich cathode, Hybrid anion- and cation-redox (HACR), Low-temperature solid-state synthesis

## INTRODUCTION

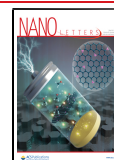
All-manganese-based Li–Mn–O cathodes are promising candidates of lithium-ion batteries<sup>1</sup> (LIB) without using expensive and toxic transition-metal (TM) elements such as Co and Ni (the price of Mn is <10% of Co and ~20% of Ni). Although they were previously thought to have low capacity and low energy density, excess Li incorporation and cation ordering (with  $\text{Li}_2\text{MnO}_3$  motifs) in Li- and Mn-rich layered cathodes (Li-rich NMC)<sup>2–5</sup> activate reversible anion redox beyond conventional transition metal redox, reaching a high capacity of >250–300 mAh/g and a high energy density of >900 Wh/kg at the active-material level at least in early cycles.<sup>1,6</sup> In such materials, Li occupies not only the Li layer as is the case in  $\text{LiCoO}_2$  and  $\text{Li}(\text{Ni}_{1-x-y}\text{Mn}_x\text{Co}_y)\text{O}_2$  (NMC) but also the TM layer with intralayer ordering between Li and TM ions. Compared to the triple axial Li–O–TM configurations centered around each O in  $\text{LiCoO}_2$  and NMC, in Li-rich NMC the octahedral O has an axial Li–O–Li configuration in addition to  $2 \times \text{Li–O–TM}$  (each O is coordinated by six cations), which makes O 2p orbitals less hybridized with TM d

orbitals, thus creating higher-energy oxygen orbitals and the ability to accept localized holes for reversible anion redox. Unfortunately, continuous voltage decay, low energy efficiency, and poor rate performance have limited the practical applications of Li-rich NMC at the present stage.<sup>7</sup> Many efforts have been undertaken to address these challenges and have shown promise through surface “immunization”<sup>8,9</sup> to deactivate labile surface oxygen and the control of lattice superstructure to suppress the formation of bulk oxygen dimers.<sup>10</sup> Nevertheless, the previous studies mainly focused on anion redox activities in layered oxides, and Co and Ni are still used both to stabilize the layered structure and to improve electronic conductivity. In comparison, Li–Mn–O has

Received: December 16, 2020

Revised: May 8, 2021

Published: May 14, 2021



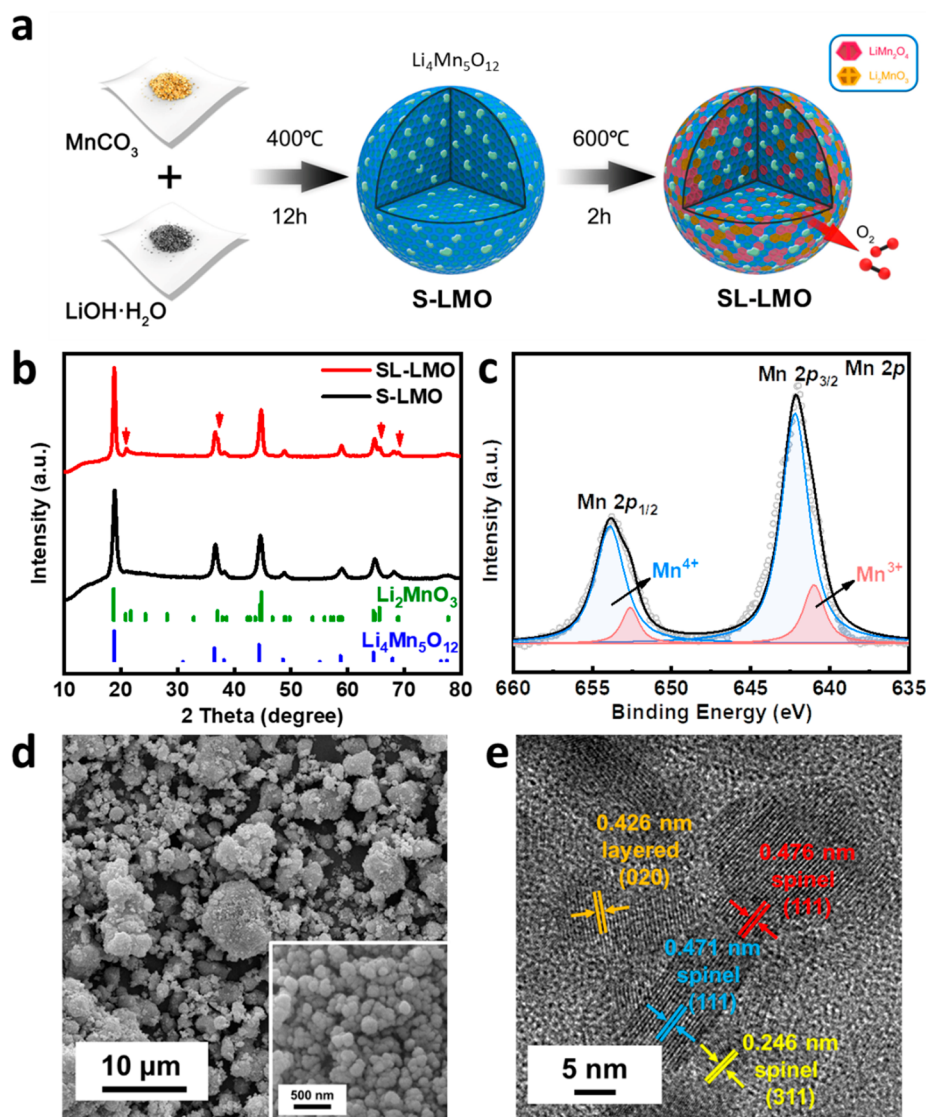


**Figure 1.** (a) Illustration of the preparation process of SL-LMO cathode (the green domains in  $\text{Li}_4\text{Mn}_5\text{O}_{12}$  illustrate amorphous areas that were observed in HRTEM image of ref 16). During the second-step calcination,  $\text{O}_2$  release would initiate from the outer surface and gradually propagate inward, rendering a possible gradient structure when a limited heat-treatment time was adopted. (b) XRD pattern of prepared S-LMO cathode and SL-LMO cathode and detailed information on  $\text{Li}_4\text{Mn}_5\text{O}_{12}$  (PDF# 46-0810) and  $\text{Li}_2\text{MnO}_3$  (PDF# 27-1252). (c) Mn 2p XPS spectra of prepared SL-LMO cathode (gray circles, observed data; blue,  $\text{Mn}^{4+}$  fitting data; red,  $\text{Mn}^{3+}$  fitting data; black, overall fitting data), where both  $\text{Mn}^{3+}$  ( $2p_{3/2}$  peak at 641.8–641.9 eV and  $2p_{1/2}$  peak at 653.4–653.7 eV<sup>22–24</sup>) and  $\text{Mn}^{4+}$  ( $2p_{3/2}$  peak at 642.2–642.7 eV and  $2p_{1/2}$  peak at 653.8–653.9 eV<sup>25,26</sup>) are observed. (d) Scanning electron microscopy images of SL-LMO cathode showing the microstructure of particles at different magnifications, (e) HRTEM of SL-LMO cathode showing four sets of interplanar spacing. We refer the HRTEM patterns with lattice spacing of 0.471 nm to spinel  $\text{Li}_4\text{Mn}_5\text{O}_{12}$  (111) plane, 0.246 nm to spinel  $\text{Li}_4\text{Mn}_5\text{O}_{12}$  (311) plane, 0.476 nm to spinel  $\text{LiMn}_2\text{O}_4$  (111) plane, and 0.426 nm to layered  $\text{Li}_2\text{MnO}_3$  (020) plane.

complicated phase diagrams and, depending on the global/local chemical compositions and the synthesis conditions, various compounds<sup>11,12</sup> can form including spinel-structure  $\text{LiMn}_2\text{O}_4$  and  $\text{Li}_4\text{Mn}_5\text{O}_{12}$  and layered-structure  $\text{Li}_2\text{MnO}_3$ .<sup>13</sup> As a result, it is important to investigate and stabilize anion redox in Li–Mn–O cathodes beyond layered structure. This sets the background for the present study, which seeks to achieve stable hybrid anion- and cation-redox (HACR) capacities in spinel-structure-based Li–Mn–O cathodes via simple solid-state synthesis and postsynthesis heat treatment.

HACR activities<sup>5,14,15</sup> in spinel-structure-based Li–Mn–O cathodes were proposed and investigated in a low-temperature-synthesized (at 400 °C)  $\text{Li}_4\text{Mn}_5\text{O}_{12}$ -like nanomaterial in our previous work,<sup>16</sup> which offers a high initial capacity of ~210

mAh/g when cycled between 1.8 and 4.7 V vs  $\text{Li}^+/\text{Li}$ . However, the material has poor cycling stability and severe gassing problem at high voltages, indicating poor stability of the anion redox. Considering the versatile structural disorders in the low-temperature-synthesized nanomaterial (e.g., Li/Mn antisite defects, surface, grain boundaries, and poor crystallinity), a possible reason for the poor cycling is the existence of high-activity near-surface oxygen, which becomes unstable upon charging and during cycling. Such oxygen instability causes side reactions with liquid electrolytes, continuous growth of cathode–electrolyte interphases (CEIs),  $\text{O}_2/\text{CO}_2$  gas evolution, and transition metal dissolution. To verify this hypothesis and to improve the cycling stability, in the present work we introduced a second aging step at 600 °C after the

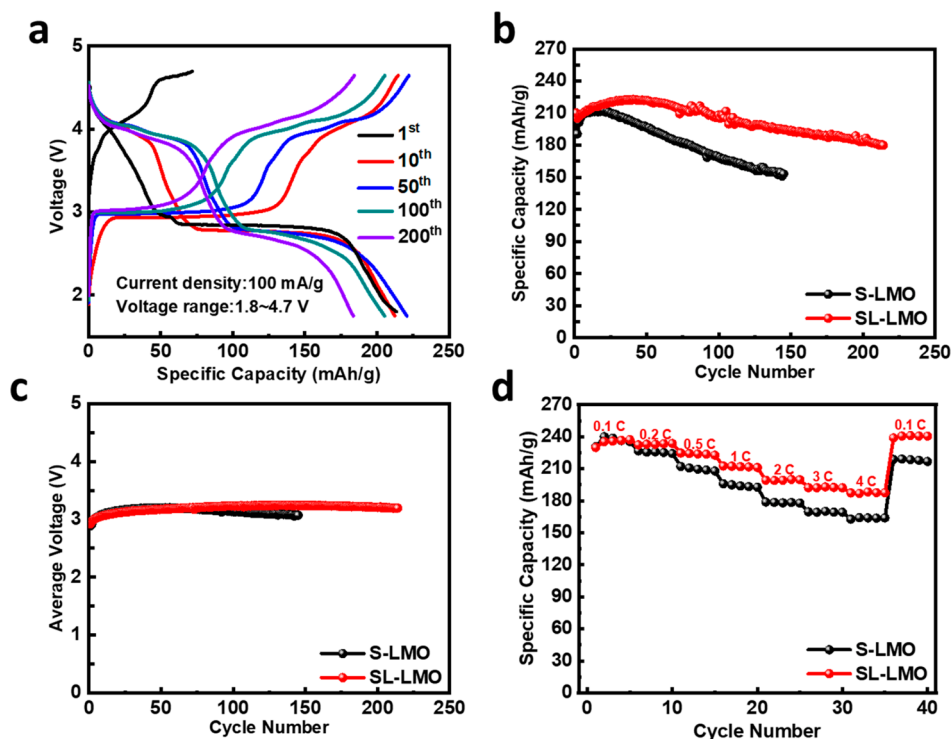
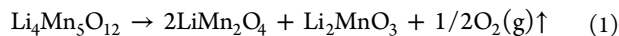


**Figure 2.** (a) Charge/discharge curves of SL-LMO cathode from the 1st cycle to the 200th cycle at a current density of 0.2 mA/cm<sup>2</sup> (about 0.5 C) between 1.8 and 4.7 V versus Li<sup>+</sup>/Li at room temperature. (b,c) Cyclic performances of SL-LMO and S-LMO cathodes: (b) specific capacity and (c) average voltage. (d) Rate performances of S-LMO and SL-LMO cathodes.

low-temperature synthesis step at 400 °C to release the high-activity oxygen according to the following chemical reaction:



Note eq 1 is an established reaction<sup>17,18</sup> that was initially discovered when investigating the complex Li–Mn–O phase diagram around Li<sub>1+x</sub>Mn<sub>2-x</sub>O<sub>4</sub> composition.<sup>19</sup> It is favored toward the right-hand side of the reaction when at high temperatures due to the larger entropy on the right-hand side from the 1/2 O<sub>2</sub>(g). Remarkably, such a pre-emptive outgassing treatment at 600 °C greatly improves the cycling stability by suppressing oxygen loss, gas release, transition-metal reduction, and impedance growth during electrochemical cycling at room temperature. As a result, the synthesized Li–Mn–O cathode can stably deliver a high discharge capacity of 225 mAh/g and an energy density of over 700 Wh/kg at a material level at a current density of 100 mA/g between 1.8 and 4.7 V vs Li<sup>+</sup>/Li, exceeding the theoretical capacity<sup>20</sup> of Li<sub>4</sub>Mn<sub>5</sub>O<sub>12</sub> (163 mAh/g) based on Mn<sup>4+</sup>/Mn<sup>3+</sup> redox couple alone. Moreover, benefiting from the suppressed side reactions and less consumption of the limited-quantity liquid electrolyte, full cells paired with Li<sub>4</sub>Ti<sub>5</sub>O<sub>12</sub> powder and Li–Sn foil anodes can survive 100 cycles and 84 cycles above 80% capacity retention, respectively, with an industrially acceptable liquid electrolyte usage of 6 g/Ah. Finally, first-principles calculations on oxygen ions without various local structures in Li<sub>4</sub>Mn<sub>5</sub>O<sub>12</sub> model structure are performed to illustrate the atomistic origin of the hypothesized high-activity oxygen.

## RESULTS AND DISCUSSION

Spinel Li<sub>4</sub>Mn<sub>5</sub>O<sub>12</sub>-like phase (referred to S-LMO hereafter) was synthesized through a simple, scalable solid-state process

at 400 °C for 12 h in air. A second-step heat treatment was conducted at 600 °C for 2 h in air to partially decompose the Li<sub>4</sub>Mn<sub>5</sub>O<sub>12</sub>-like phase into spinel LiMn<sub>2</sub>O<sub>4</sub> and layered Li<sub>2</sub>MnO<sub>3</sub> (referred to SL-LMO hereafter). As shown in Figure 1b, while the X-ray diffraction (XRD) pattern of S-LMO matches well with spinel Li<sub>4</sub>Mn<sub>5</sub>O<sub>12</sub> phase, additional peaks exist in the XRD pattern of SL-LMO and they match with layered Li<sub>2</sub>MnO<sub>3</sub> structure. High-temperature in situ XRD (Figure S1) confirms the reaction mechanism eq 1, where Li<sub>2</sub>MnO<sub>3</sub>-type ordering begins to form at 400 °C and becomes stable after 2 h at 600 °C. Both S-LMO and SL-LMO have broadened XRD peaks, indicating nanoscale particle sizes and poor crystallinity, which is also evidenced by the following microscopy characterizations. While nanoparticles can enhance kinetics and promote anion-redox capacity due to surface disorder, the side reactions at electrochemically active surfaces would consume the precious electrolyte. They also make oxygen loss and gassing a most challenging problem for such a large surface-area-to-volume-ratio electrode, especially under industrial conditions where the electrolyte quantity is highly limited (2–6 g/Ah, often less than the cathode weight).

We next conducted X-ray photoelectron spectroscopy (XPS) measurements to confirm the existence of both Li<sub>4</sub>Mn<sub>5</sub>O<sub>12</sub> and LiMn<sub>2</sub>O<sub>4</sub> phases in SL-LMO. Note that while the spinel Li<sub>4</sub>Mn<sub>5</sub>O<sub>12</sub> and LiMn<sub>2</sub>O<sub>4</sub> have very similar XRD patterns that can hardly be distinguishable for nanomaterials with broadened peaks, Mn is +4 valence in Li<sub>4</sub>Mn<sub>5</sub>O<sub>12</sub> and is +3.5 (i.e., 50% + 3 and 50% + 4) in LiMn<sub>2</sub>O<sub>4</sub>. As shown by Mn 2p spectra in Figure 1c, SL-LMO contains both Mn<sup>3+</sup> and Mn<sup>4+</sup>, and quantitative analysis (Figure S2) suggests a Mn<sup>3+</sup>/Mn<sup>4+</sup> ratio of 0.24 in SL-LMO. Furthermore, Figure 1d reveals that after 2 h of treatment at 600 °C, submicron agglomerations of fine nanoparticles are formed, which would

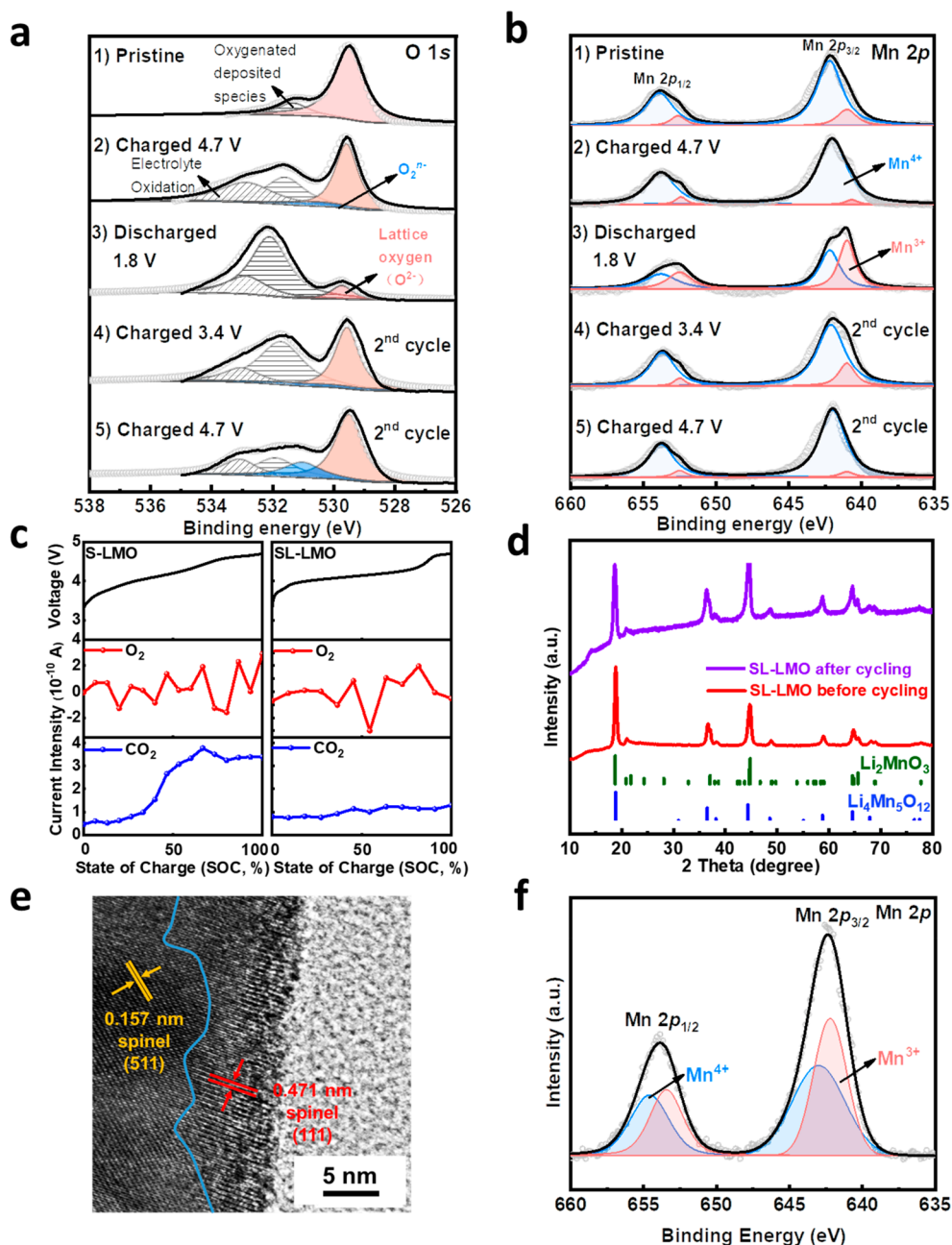


**Figure 3.** (a) O 1s XPS spectra at various states of electrochemical cycling. The red curve with the peak at 529.5 eV represents the  $O^{2-}$  anions of the crystalline network<sup>27</sup> and the weakly absorbed surface species, and blue curve at  $\sim 530.5$  eV<sup>27</sup> is attributed to  $O_2^{\bullet-}$ , whereas the two gray striped areas with the peaks at 532.1 and 533.2 eV are related to the oxygenated deposited species and electrolyte decomposition products.<sup>28</sup> (b) Mn 2p XPS spectra where the red and blue peaks represent  $Mn^{3+}$  and  $Mn^{4+}$  respectively. The peaks at 642.58 and 653.88 eV are characteristic peaks of  $Mn^{4+} 2p_{3/2}$  and  $Mn^{4+} 2p_{1/2}$ , respectively, and the peaks at 641.85 and 653.40 eV correspond to  $Mn^{3+} 2p_{3/2}$  and  $Mn^{3+} 2p_{1/2}$ . (c) DEMS analysis of the SL-LMO and S-LMO cathodes in a half cell tested with a constant current density of 100 mA/g when charging to 4.7 V in the first cycle. (d) XRD patterns of the SL-LMO cathode after and before cycling and detailed information on  $Li_4Mn_5O_{12}$  (PDF# 46-0810) and  $Li_2MnO_3$  (PDF# 27-1252). (e) TEM image of SL-LMO cathode material at near-surface region after cycling. (f) Mn 2p XPS spectra of the SL-LMO material after cycling (gray circles, observed data; blue,  $Mn^{4+}$  fitting data; red,  $Mn^{3+}$  fitting data; black, overall fitting data).

benefit the electrochemical performance from several aspects: (1) help accommodate strain through slippages at the grain boundaries<sup>21</sup> and phase boundaries; (2) decrease the contact area with electrolyte and thus reduce the parasitic side reactions. Note that such a self-agglomerated microstructure offers a relatively high compact density of 2.8 g/cm<sup>3</sup> (Table S1) for SL-LMO, slightly lower than that of NCM (3.2–3.5 g/cm<sup>3</sup>) but higher than that of  $LiFePO_4$  (2.2–2.4 g/cm<sup>3</sup>) that has already been heavily optimized at the industry level. Lastly,

the crystal structure was characterized by high-resolution TEM (HRTEM) (Figure 1e), where both crystalline and disordered amorphous-like regions are detected. With reference diffraction data in Table S2, the coexistence of three phases in reaction eq 1 is confirmed both at the surface (Figure S3) and in the bulk (Figure 1e).

The cycling performance of SL-LMO was evaluated in Figure 2a–c, where a gradual increase in discharge capacity (e.g., so-called activation) is observed in the first 50 cycles. A

high discharge capacity of 225 mAh/g and a high discharge energy density of over 700 Wh/kg at a material level were achieved after ~50 cycles' activation at room temperature, and 214 stable cycles have been maintained at 80% capacity retention. It is interesting to notice that more high-voltage capacity above 4 V is activated upon cycling, implying the increased capacity possibly contributed by high-voltage oxygen redox. This may be due to lattice rearrangements during electrochemical cycling that makes some oxygen redox states thermodynamically or kinetically more accessible below 4.7 V. Accordingly, the average discharge voltage increases in the first 50 cycles (Figure 2c), and a similar trend was also found in S-LMO cathode. However, in contrast with the voltage decay of S-LMO cathode after the first 50 cycles, SL-LMO maintains a stable discharge voltage of ~3.2 V thereafter. Interestingly, akin to the sloping voltage curve in the first charge of S-LMO, SL-LMO exhibits more obvious voltage plateau feature, which indicates that after higher-temperature treatment at 600 °C the atomic arrangement of SL-LMO is more ordered than that of S-LMO and thus the structure of SL-LMO is more stable than that of S-LMO, which remits the voltage decay. Cyclic voltammetry (CV, Figure S4) measurements further reveal that with prolonged cycling, the peak area at high voltage increases in the charging process, indicating an activation process of anionic capacity with cycles. (Also note the voltage profile of SL-LMO in Figure 2a is much more slopy than that of LiMn<sub>2</sub>O<sub>4</sub>.<sup>26</sup> Accordingly, the capacity is contributed more by the redox states outside of the peak regions in Figure S4, which is fundamentally different from the case of LiMn<sub>2</sub>O<sub>4</sub>. This may be due to the degenerate energy states from both cation and anion redox and from the versatile defects of the multiphase nanocomposite.) Concomitantly, the average discharge voltage exhibits a continuously climbing trend in the first several dozens of cycles. Such "rejuvenation" phenomenon could be attributed to an O-redox induced disruption of local structural order and associated volume expansion, which reduces the lithium-ion transport resistance in the cathode materials.<sup>9</sup> This argument of better kinetics is also supported by better rate performance of SL-LMO than S-LMO as shown in Figure 2d.

In order to better understand the redox process, XPS measurements (Figure 3a,b) were conducted at the surface of the pristine SL-LMO and variously charged/discharged samples. In the pristine state, Mn starts with hybrid +4 and +3 states and its average valence is ~3.8. When first charged to 4.7 V versus Li<sup>+</sup>/Li, most Mn<sup>3+</sup> is oxidized to Mn<sup>4+</sup> (Figure 3b), suggesting contribution of Mn<sup>3+</sup> in LiMn<sub>2</sub>O<sub>4</sub> to the charge capacity. For O 1s spectrum in Figure 3a, the red fitting curve at 529.5 eV can be attributed to O<sup>2-</sup> anions of the crystalline network,<sup>27</sup> and the two shaded fitting curves at 532.1 and 533.2 eV can be attributed to the oxygenated deposited species and electrolyte decomposition products.<sup>28</sup> However, an additional signal can be found at ~530.5 eV (the blue fitting curve) for the 4.7 V charged sample, which can be attributed to oxidized oxygen ion or peroxo-like species.<sup>27</sup> After discharge to 1.8 V, over 50% Mn<sup>4+</sup> is reduced to Mn<sup>3+</sup> and the O 1s signal at ~530.5 eV diminishes. During a second charge, Mn<sup>3+</sup> is gradually oxidized and most Mn is at +4 valence when charged to 4.7 V. Meanwhile, the signal of peroxo-like species becomes much stronger than at the first charge state at 4.7 V, suggesting more contribution from anion redox after the first cycle. The above observations support active anion redox at the surface and we next seek to characterize the anion redox in the bulk. We first conducted depth-profiling XPS analysis of the pristine

sample, and the samples charged to 4.7 V and discharged to 1.8 V after 10 cycles. All of the samples were etched by 50 nm from the surface by sputtering and analyzed by XPS (Figure S6). Consistent with the XPS results on the surface, an additional signal can be found at ~530.5 eV (the blue fitting curve in Figure S6a) for the peroxo-like species in the 4.7 V charged sample. For Mn 2p (Figure S6b) in the bulk, we also confirmed mixed Mn<sup>3+</sup> and Mn<sup>4+</sup> in the pristine sample, mainly Mn<sup>4+</sup> in the 4.7 V charged sample, and mainly Mn<sup>3+</sup> in the 1.8 V discharged sample, which again agree with the surface XPS results. Lastly, we conducted soft X-ray absorption spectroscopy (sXAS) of O K-edge and Mn L-edge using the partial fluorescence yield (PFY) mode, which has a detection depth of more than 100 nm into the particle<sup>29</sup> and is thus a suitable technique to probe anion redox in the bulk. As shown in Figure S7, when charged to 4.7 V in the first (red curve) and second cycle (purple curve), the samples show slightly higher intensity at ~530.5–531.5 eV, a feature of anion redox,<sup>30,31</sup> than the pristine sample, but obviously lower than what is usually observed in Li-rich layered cathodes.<sup>32</sup> Meanwhile, a little peak shift at ~590.0 eV is observed, which generally indicates a change in the metal–oxygen hybridization upon charging, as O–K XAS pre-edge reflects overlapping cation–anion features.<sup>33,34</sup> In conjunction with the direct probes of Mn 3d states in Mn–L XAS (Figure S7) where no obvious variation in Mn states is detected, it is reasonable to speculate the change in metal–oxygen hybridization should be at least partially attributed to oxygen-redox activity. This anticipation is further supported by DFT calculations. Comparing the calculated total density of states (DOS) and projected DOS of O 2p and Mn 3d states for Li<sub>4</sub>Mn<sub>5</sub>O<sub>12</sub>, Li<sub>3.5</sub>Mn<sub>5</sub>O<sub>12</sub>, and Li<sub>3</sub>Mn<sub>5</sub>O<sub>12</sub> (Figure S8), Li removal is mostly contributed by change in the occupancy of O 2p states (contributing 88% for 0.5 electron removal in Li<sub>3.5</sub>Mn<sub>5</sub>O<sub>12</sub> and 82% for 1 electron removal in Li<sub>3</sub>Mn<sub>5</sub>O<sub>12</sub>). More generally speaking, while O–O dimer formation may be unavoidable if too much oxygen redox is used (~150 mAh/g capacity from oxygen redox in Li-rich layered cathodes), changes in O 2p states or O 2p–Mn 3d hybrid states could be sufficient to compensate the Li removal in our case (where we estimated less than ~80 mAh/g of oxygen redox is used). This low usage of oxygen redox could be another reason why the changes in O–K XAS are not as obvious as the case in Li-rich layered cathodes.

To understand the improved electrochemical stability, we measured the gas generation during the first charge cycle using differential electrochemical mass spectrometry (DEMS). As shown in Figure 3c, much less CO<sub>2</sub> was generated by SL-LMO than S-LMO. This supports our preemptive immunization mechanism since CO<sub>2</sub> is produced by the oxidation of the carbonate electrolyte when encountering reactive oxygen at charged cathode surfaces. The suppressed O<sub>2</sub> generation is also identified though the data are more noisy. In addition, post-mortem characterizations were conducted after 214 cycles to understand the degradation mechanism. From the XRD patterns in Figure 3d, the peaks are broadened after cycling, indicating defect generation and microstructural degradation during electrochemical cycling. From the refinement results in Figure S2, the mass ratios of Li<sub>4</sub>Mn<sub>5</sub>O<sub>12</sub>, LiMn<sub>2</sub>O<sub>4</sub>, and Li<sub>2</sub>MnO<sub>3</sub> are 49%, 36%, and 15% before cycling, and 52%, 37%, and 11% after cycling, respectively. The decrease in mass ratio of Li<sub>2</sub>MnO<sub>3</sub> and increase in that of LiMn<sub>2</sub>O<sub>4</sub> can be attributed to phase transition from layered structure to spinel structure during cycling. This weakened Li<sub>2</sub>MnO<sub>3</sub>-like ordering

is also consistent with our TEM data, where the lattice pattern of  $\text{Li}_2\text{MnO}_3$  becomes weaker near the surface (Figure 3e). According to the XPS pattern (Figure 3f), there are still  $\text{Mn}^{3+}$  ions in the material after cycles, which proves the existence of  $\text{LiMn}_2\text{O}_4$ . Additionally, the TEM images at near-surface regions (Figure 3e) also corroborate this fact clearly, where no lattice spacing that matches with layered  $\text{Li}_2\text{MnO}_3$  could be identified anymore, indicating the disappearance of  $\text{Li}_2\text{MnO}_3$ ; instead, there are only mixture phases of spinel structure. All of these suggest that phase transition takes place during cycling, and layered  $\text{Li}_2\text{MnO}_3$  phase at the near-surface region transforms into spinel  $\text{LiMn}_2\text{O}_4$  phase.<sup>6,35</sup> Indeed, similar observations have been reported by other research groups,<sup>36</sup> and two factors contributing to the atomistic kinetics and driving force for such transformation from layered structure to spinel phases upon electrochemical cycling have been proposed. First of all, there is an intrinsic structural correlation between layered and spinel patterns that makes TM ions' migration from TM layer to Li layer both thermodynamically and kinetically favorable at highly charged states. Specifically, as TM ions are usually more reduced in the (near) surface region of cycled cathodes due to anion-redox-induced oxygen mobility and oxygen loss, a larger amount of Mn being +4 would be left at the surface during charging. Since ionic radii of  $\text{Mn}^{4+}$  (67 pm) and  $\text{Li}^+$  (68 pm) are similar, Mn being +4 valence tends to migrate into the Li layer, which is almost empty in highly charged states. Besides, electrostatic repulsion between TM ions is prone to separate them apart, maximizing their distance and offering a driving force for cations to rearrange into a cubic spinel structure,  $\text{AB}_2\text{O}_4$ , where B-site cations only occupy half of the octahedral sites in an edge-sharing manner. Luckily, the surface phase reconstruction happens in a good way because the "good spinel" phase  $\text{Li}(\text{TM})_2\text{O}_4$  instead of "bad spinel"<sup>13</sup> phase like  $(\text{TM})_3\text{O}_4$  are generated. The newly formed  $\text{LiMn}_2\text{O}_4$ , together with the as-synthesized  $\text{LiMn}_2\text{O}_4$  could serve as a shield to protect the internal  $\text{Li}_4\text{Mn}_5\text{O}_{12}$  as well as  $\text{Li}_2\text{MnO}_3$  phases, shutting down the percolating pathway of oxygen ions to the electrolyte, trapping oxygen in the bulk particles and restricting its global mobility (the concept of "solid oxygen").<sup>8</sup> Therefore, performance can be improved with cycling, as revealed in Figure 2b,c. It is worth mentioning that  $\text{LiMn}_2\text{O}_4$  shell also reduces the cell impedance, as revealed in the electrochemical impedance spectroscopy (EIS) in Figure S5.

Generally speaking, a big concern for voltage fading in Li-rich cathodes is oxygen loss that promotes side reactions and surface and bulk phase transformations.<sup>13</sup> For SL-LMO cathode, the surfaces have been immunized preventively under a controlled and relatively brief high-temperature treatment with the lattice simultaneously reconstructing and the point defects (e.g., oxygen lattice vacancy) annealed out. This pre-empted the excess oxygen escape, lattice defects, and collapse that would have been generated in later electrochemical cycling at room temperature, which can be likened to an ordered army retreat instead of a rout, or a vaccination treatment, given that oxygen will have to become more mobile<sup>8,37</sup> as  $\text{O}^{1-}$ , so it would be better to deplete high-activity oxygen near the surface to better confine them in the interior. In room-temperature cycling, any oxygen escaping from the surface would leave an oxygen vacancy behind, accelerating further interior oxygen mobility. This eventually leads to structural rout. The thermal immunization treatment allows the near-surface oxygen to escape, leading to an oxygen-poor

surface according to (1) but also with well-annealed surface structure with no excess defects due to 600 °C annealing, while the interior maintains a higher fraction of retained  $\text{Li}_4\text{Mn}_5\text{O}_{12}$  (Figure 1a) that has shown HACR capacity.<sup>16</sup>

On account of the microstructural improvement of our SL-LMO cathode, one can expect a decent full-cell cycling performance under lean electrolyte. When paired with  $\text{Li}_4\text{Ti}_5\text{O}_{12}$  anode, the SL-LMO cathode can be charged to 217 mAh/g and then discharged to 207 mAh/g in the first cycle, giving a 95.4% initial Coulombic efficiency (ICE) (Figure 4a). After five cycles' adaption in the system, the cell

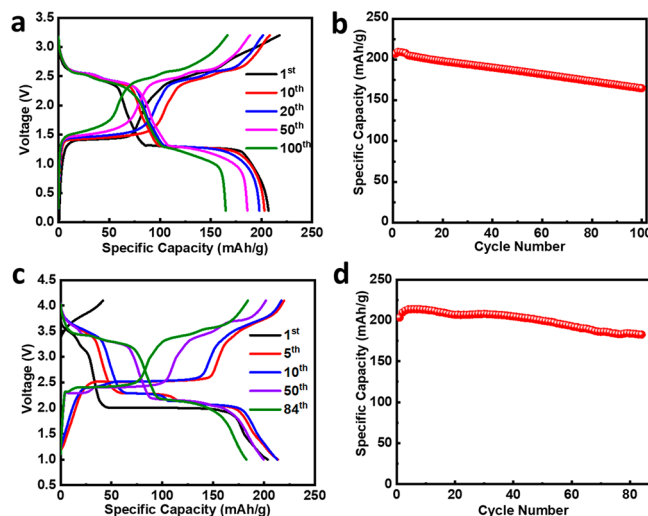


**Figure 4.** (a) Charge/discharge curves of SL-LMO// $\text{Li}_4\text{Ti}_5\text{O}_{12}$  full cells (negative to positive ratio N:P of 1.1) with 6 g/Ah of standard carbonate-based electrolyte, not too far from that used in industrial batteries. Note that our SL-LMO cathode material is prelithiated in half cells through electrochemical methods for the pristine state of the material is inactivated and short of lithium ions, (b) specific capacity cycling performance of the full cell in 100 cycles in the first 5 cycles at a current density 0.04 mA/cm<sup>2</sup> (about 0.1 C) and then at a current density of 0.08 mA/cm<sup>2</sup>. (c) Charge/discharge curves of SL-LMO cathode (areal capacity of 2.7 mAh/cm<sup>2</sup>) with mechanical prelithiated Sn anode ( $\text{Li}_x\text{Sn}$  alloy) in pouch cells, (d) cycling performance of the SL-LMO// $\text{Li}_x\text{Sn}$  full cells.

can deliver a reversible capacity of 205.3 mAh/g at a current density of 0.08 mA/cm<sup>2</sup> (about 0.2 C). Even under such a challenging lean-electrolyte condition, the full cell can still survive over 100 cycles with a discharge capacity intention of 80% of the initial capacity (Figure 4b). Similarly, using the same electrolyte quantity, we also assemble a SL-LMO// $\text{Li}_x\text{Sn}$  full pouch cell (Figure 4c) with 0.5× lithium excess and the cell performance could be found in Figure 4d. On the basis of the cathode-active material weight, an initial specific capacity of 203.5 mAh/g was obtained and the cycling could maintain stability in the next 83 cycles. The full-cell energy is estimated to be 316 Wh/kg, and energy density of the total battery achieves 307 Wh/kg; the battery configuration of SL-LMO// $\text{Li}_x\text{Sn}$  full cell in terms of weight percentage is shown in Figure S9.

The experimental results above show active anion redox in  $\text{Li}_4\text{Mn}_5\text{O}_{12}$ -like S-LMO and  $\text{Li}_4\text{Mn}_5\text{O}_{12}$ - $\text{LiMn}_2\text{O}_4$ - $\text{Li}_2\text{MnO}_3$  nanocomposite SL-LMO in contrast to electrochemically inaccessible oxygen states in "conventional"  $\text{Li}_4\text{Mn}_5\text{O}_{12}$ . The poor cycling of S-LMO and improved stability of SL-LMO after the second calcination step also suggest high-activity

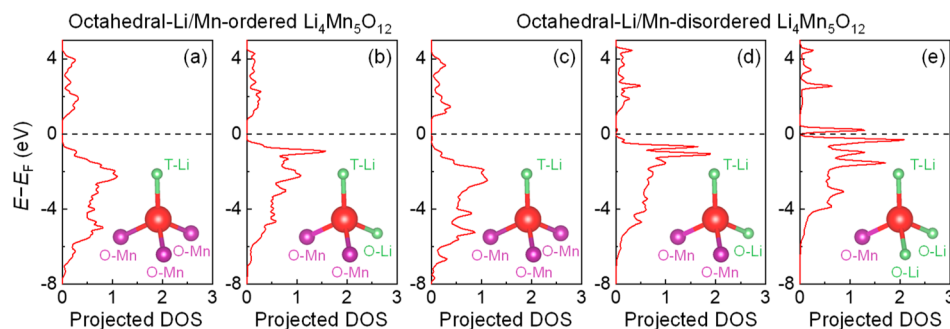


**Figure 5.** Projected DOS of oxygen ions in octahedral-Li/Mn-ordered  $\text{Li}_4\text{Mn}_5\text{O}_{12}$  coordinated (a) by three octahedral Mn and one tetrahedral Li, and (b) by two octahedral Mn, one octahedral Li, and one tetrahedral Li, as compared with projected DOS of oxygen ions in octahedral-Li/Mn-disordered  $\text{Li}_4\text{Mn}_5\text{O}_{12}$  coordinated (c) by three octahedral Mn and one tetrahedral Li, (d) by two octahedral Mn, one octahedral Li, and one tetrahedral Li, and (e) by one octahedral Mn, two octahedral Li, and one tetrahedral Li. Dashed lines indicate the Fermi level  $E_F$ . Insets: schematic local atomic structures around oxygen ions.

oxygen that can be released electrochemically or chemically. These observations indicate that oxygen ions in S-LMO and SL-LMO have distributed redox energy levels, which could arise from their distinct local structures and defective lattice under nonequilibrium synthesis conditions. This is shown by the following first-principles calculations. In “conventional” spinel-structure  $\text{Li}_4\text{Mn}_5\text{O}_{12}$ , three Li sit in the tetrahedral sites, and one Li and five Mn sit in the octahedral sites in an ordering manner. As a result, oxygen ions are either coordinated by three octahedral Mn and one tetrahedral Li (Figure 5a) or by two octahedral Mn, one octahedral Li, and one tetrahedral Li (Figure 5b). As shown by the projected density of states (DOS) in Figure 5a,b, the latter has more occupied high-energy oxygen 2p states close to the Fermi level  $E_F$  than the former, because more O–Mn bonds and hence more hybridization between O 2p and Mn 3d orbitals. Yet neither oxygen ion is electrochemically active at least below 4.8 V versus  $\text{Li}^+/\text{Li}$ . In comparison, if we break down the cation ordering and create octahedral-Li/Mn-disordered  $\text{Li}_4\text{Mn}_5\text{O}_{12}$ , oxygen ions would be coordinated (i) by three octahedral Mn and one tetrahedral Li (Figure 5c), (ii) by two octahedral Mn, one octahedral Li, and one tetrahedral Li (Figure 5d), (iii) by one octahedral Mn, two octahedral Li, and one tetrahedral Li (Figure 5e), or (iv) by three octahedral Li and one tetrahedral Li (statistically having a low possibility to form under 1:5 octahedral Li/Mn ratio). While the projected DOS of type-i and type-ii oxygen ions are similar to the corresponding ones in octahedral-Li/Mn-ordered  $\text{Li}_4\text{Mn}_5\text{O}_{12}$  (demonstrating the robustness of the analyzing approach to correlate local atomic and electronic structures<sup>38–40</sup>), high-activity oxygen ion is identified in Figure 5e with some unoccupied oxygen 2p states above  $E_F$  even in its fully lithiated form. In real materials, the variations in local structure and bonding can be further complicated with vacancies and other lattice defects in SL-LMO nanoparticles, which would then create a broad, continuous, active oxygen-redox band (Figure S10, contributed mainly by O 2p states and partially by hybridized Mn 3d states). This picture is fully consistent with our experimental findings of active anion redox. However, one should realize that the activity and stability of anion redox are competing with each other and they have to be balanced to achieve long-term cyclability. In this sense, while S-LMO contains many defects from grain boundaries, interfaces, and lattice defects and has active oxygen redox, it also suffers from extensive oxygen loss and fast degradations as can be seen from the DEMS and electrochemical data. In comparison, SL-LMO does better by

releasing the “over-active” near-surface oxygen species in the composite. Therefore, oxygen activity and stability are better balanced and the key in practice is to make full use of electrochemically active oxygen states in the interior and to prerelease those near the surface with extremely high reactivity toward the electrolyte.

## CONCLUSION

We have developed a scalable low-temperature solid-state synthesis to prepare a three-phase  $\text{Li}_4\text{Mn}_5\text{O}_{12}$ – $\text{LiMn}_2\text{O}_4$ – $\text{Li}_2\text{MnO}_3$  nanocomposite. Benefiting from the second-step heat treatment that promotes the leaching of near-surface high-activity oxygen before electrochemical cycling, such nano-architected spinel/layered Li-rich cathode material can deliver a high capacity over 225 mAh/g and maintains 214 stable cycles at 80% capacity retention. Because of the suppressed unwanted reactions with electrolyte with an industrially acceptable electrolyte injection amount (6 g/Ah), the full cell with  $\text{Li}_4\text{Ti}_5\text{O}_{12}$  can still deliver 100 cycles, which proves the two-step heat treatment to be effective for immunizing against HACR induced global oxygen mobility and oxygen release. The cheap cost and satisfactory energy density and cycle life suggest that such Li–Mn–O HACR cathode could be a competitive next-generation cathode material.

## ASSOCIATED CONTENT

### Supporting Information

The Supporting Information is available free of charge at <https://pubs.acs.org/doi/10.1021/acs.nanolett.0c04920>.

Experiment section, simulations, calculation and supplementary results (PDF)

## AUTHOR INFORMATION

### Corresponding Authors

Sa Li – School of Materials Science and Engineering and Institute of New Energy for Vehicles, Tongji University, Shanghai 201804, China; Email: [lisa@tongji.edu.cn](mailto:lisa@tongji.edu.cn)

Yanhao Dong – Department of Nuclear Science and Engineering, Massachusetts Institute of Technology, Cambridge, Massachusetts 02139, United States; Email: [dongyh@mit.edu](mailto:dongyh@mit.edu)

Ju Li – Department of Nuclear Science and Engineering and Department of Materials Science and Engineering, Massachusetts Institute of Technology, Cambridge,

Massachusetts 02139, United States; [orcid.org/0000-0002-7841-8058](https://orcid.org/0000-0002-7841-8058); Email: [liju@mit.edu](mailto:liju@mit.edu)

## Authors

**Xin Sun** – School of Materials Science and Engineering and Institute of New Energy for Vehicles, Tongji University, Shanghai 201804, China

**Yang Liu** – School of Materials Science and Engineering and Institute of New Energy for Vehicles, Tongji University, Shanghai 201804, China

**Guang Liu** – School of Materials Science and Engineering and Institute of New Energy for Vehicles, Tongji University, Shanghai 201804, China

**Weijiang Xue** – Department of Nuclear Science and Engineering, Massachusetts Institute of Technology, Cambridge, Massachusetts 02139, United States; [orcid.org/0000-0002-3060-4580](https://orcid.org/0000-0002-3060-4580)

**Iradwikanari Waluyo** – National Synchrotron Light Source II, Brookhaven National Laboratory, Upton, New York 11973, United States; [orcid.org/0000-0002-4046-9722](https://orcid.org/0000-0002-4046-9722)

**Zhi Zhu** – Department of Nuclear Science and Engineering, Massachusetts Institute of Technology, Cambridge, Massachusetts 02139, United States

**Yunguang Zhu** – Research Laboratory of Electronics, Massachusetts Institute of Technology, Cambridge, Massachusetts 02139, United States; [orcid.org/0000-0003-3884-4359](https://orcid.org/0000-0003-3884-4359)

**Yunhui Huang** – School of Materials Science and Engineering and Institute of New Energy for Vehicles, Tongji University, Shanghai 201804, China

Complete contact information is available at:

<https://pubs.acs.org/10.1021/acs.nanolett.0c04920>

## Notes

The authors declare no competing financial interest.

## ACKNOWLEDGMENTS

S.L., X.S., Y.L., G.L., and Y.H. are grateful for the support from the National Natural Science Foundation of China (NSFC-Nos. 91934304, 51632001, and 51972236). J.L. and Y.D. acknowledge support from NSF CBET-2034902.

## REFERENCES

- (1) Armstrong, A. R.; Bruce, P. G. Synthesis of layered  $\text{LiMnO}_2$  as an electrode for rechargeable lithium batteries. *Nature* **1996**, *381*, 499–500.
- (2) Gummow, R.; De Kock, A.; Thackeray, M. Improved capacity retention in rechargeable 4 V lithium/lithium manganese oxide (spinel) cells. *Solid State Ionics* **1994**, *69*, 59–67.
- (3) Sathiyaraj, M.; Rousse, G.; Ramesha, K.; Laisa, C. P.; Vezin, H.; Sougrati, M. T.; Doublet, M.-L.; Foix, D.; Gonbeau, D.; Walker, W.; Prakash, A. S.; Ben Hassine, M.; Dupont, L.; Tarascon, J.-M.; Prakash, A. S.; Ben Hassine, M.; Dupont, L.; Tarascon, J.-M. Reversible anionic redox chemistry in high-capacity layered-oxide electrodes. *Nat. Mater.* **2013**, *12*, 827–835.
- (4) Myung, S. T.; Lee, K. S.; Kim, D. W.; Scrosati, B.; Sun, Y. K. Spherical core-shell  $\text{Li}[(\text{Li}_{0.05}\text{Mn}_{0.95})_{0.8}(\text{Ni}_{0.25}\text{Mn}_{0.75})_{0.2}]_2\text{O}_4$  spinels as high performance cathodes for lithium batteries. *Energy Environ. Sci.* **2011**, *4*, 935–939.
- (5) Johnson, C.; Kim, J.; Lefief, C.; Li, N.; Vaughey, J.; Thackeray, M. The significance of the  $\text{Li}_2\text{MnO}_3$  component in ‘composite’  $x\text{Li}_2\text{MnO}_3 \cdot (1-x)\text{LiMn}_{0.5}\text{Ni}_{0.5}\text{O}_2$  electrodes. *Electrochem. Commun.* **2004**, *6*, 1085–1091.
- (6) Thackeray, M.; Kang, S. H.; Johnson, C. S.; Vaughey, J. T.; Benedek, R.; Hackney, S.  $\text{Li}_2\text{MnO}_3$ -stabilized  $\text{LiMO}_2$  (M = Mn, Ni,

Co) electrodes for lithium-ion batteries. *J. Mater. Chem.* **2007**, *17*, 3112–3125.

(7) Berg, E. J.; Villeveille, C.; Streich, D.; Trabesinger, S.; Novák, P. Rechargeable batteries: grasping for the limits of chemistry. *J. Electrochem. Soc.* **2015**, *162*, A2468.

(8) Zhu, Z.; Yu, D.; Yang, Y.; Su, C.; Huang, Y.; Dong, Y.; Waluyo, I.; Wang, B.; Hunt, A.; Yao, X.; Lee, J.; Xue, W.; Li, J.; Lee, J.; Xue, W.; Li, J. Gradient Li-rich oxide cathode particles immunized against oxygen release by a molten salt treatment. *Nat. Energy* **2019**, *4*, 1049–1058.

(9) Lee, J.; Yu, D.; Zhu, Z.; Yao, X.; Wang, C.; Dong, Y.; Malik, R.; Li, J. Kinetic rejuvenation of Li-rich Li-ion battery cathodes upon oxygen redox. *ACS Appl. Energy Mater.* **2020**, *3*, 7931–7943.

(10) House, R. A.; Maitra, U.; Perez-Osorio, M. A.; Lozano, J. G.; Jin, L.; Somerville, J. W.; Duda, L. C.; Nag, A.; Walters, A.; Zhou, K.-J.; Roberts, M. R.; Bruce, P. G.; Roberts, M. R.; Bruce, P. G. Superstructure control of first-cycle voltage hysteresis in oxygen-redox cathodes. *Nature* **2020**, *577*, 502–508.

(11) Liddle, B. J.; Collins, S. M.; Bartlett, B. M. A new one-pot hydrothermal synthesis and electrochemical characterization of  $\text{Li}_{1+x}\text{Mn}_{2-x}\text{O}_4$  spinel structured compounds. *Energy Environ. Sci.* **2010**, *3*, 1339–1346.

(12) Mukai, K.; Kishida, Y.; Nozaki, H.; Dohmae, K. Thermal expansion in lithium manganese oxide spinels  $\text{Li}[\text{Li}_x\text{Mn}_{2-x}]\text{O}_4$  with  $0 \leq x \leq 1/3$ . *J. Power Sources* **2013**, *224*, 230–235.

(13) Huang, Y.; Dong, Y.; Li, S.; Lee, J.; Wang, C.; Zhu, Z.; Xue, W.; Li, Y.; Li, J. Lithium manganese spinel cathodes for lithium-ion batteries. *Adv. Energy Mater.* **2021**, *11*, 2000997.

(14) Armstrong, A. R.; Holzapfel, M.; Novák, P.; Johnson, C. S.; Kang, S. H.; Thackeray, M.; Bruce, P. G. Demonstrating oxygen loss and associated structural reorganization in the lithium battery cathode  $\text{Li}[\text{Ni}_{0.2}\text{Li}_{0.2}\text{Mn}_{0.6}]\text{O}_2$ . *J. Am. Chem. Soc.* **2006**, *128*, 8694–8698.

(15) Yabuuchi, N.; Yoshii, K.; Myung, S. T.; Nakai, I.; Komaba, S. Detailed studies of a high-capacity electrode material for rechargeable batteries,  $\text{Li}_2\text{MnO}_3$ - $\text{LiCo}_{1/3}\text{Ni}_{1/3}\text{Mn}_{1/3}\text{O}_2$ . *J. Am. Chem. Soc.* **2011**, *133*, 4404–4419.

(16) Liu, Y.; Liu, G.; Xu, H.; Zheng, Y.; Huang, Y.; Li, S.; Li, J. Low-temperature synthesized  $\text{Li}_4\text{Mn}_5\text{O}_{12}$ -like cathode with hybrid cation- and anion-redox capacities. *Chem. Commun.* **2019**, *55*, 8118–8121.

(17) Thackeray, M.; Mansuetto, M.; Johnson, C. Thermal stability of  $\text{Li}_4\text{Mn}_5\text{O}_{12}$  electrodes for lithium batteries. *J. Solid State Chem.* **1996**, *125*, 274–277.

(18) Thackeray, M.; David, W.; Bruce, P.; Goodenough, J. Lithium insertion into manganese spinels. *Mater. Res. Bull.* **1983**, *18*, 461–472.

(19) Gao, Y.; Dahn, J. The high temperature phase diagram of  $\text{Li}_{1+x}\text{Mn}_{2-x}\text{O}_4$  and its implications. *J. Electrochem. Soc.* **1996**, *143*, 1783.

(20) Thackeray, M.; De Kock, A.; Rossouw, M.; Liles, D.; Bittihn, R.; Hoge, D. Spinel electrodes from the Li-Mn-O system for rechargeable lithium battery applications. *J. Electrochem. Soc.* **1992**, *139*, 363.

(21) Armstrong, A. R.; Paterson, A. J.; Robertson, A. D.; Bruce, P. G. Nonstoichiometric layered  $\text{Li}_x\text{Mn}_y\text{O}_2$  with a high capacity for lithium intercalation/deintercalation. *Chem. Mater.* **2002**, *14*, 710–719.

(22) Spahr, M. E.; Novák, P.; Schnyder, B.; Haas, O.; Nesper, R. Characterization of layered lithium nickel manganese oxides synthesized by a novel oxidative coprecipitation method and their electrochemical performance as lithium insertion electrode materials. *J. Electrochem. Soc.* **1998**, *145*, 1113.

(23) Di Castro, V.; Polzonetti, G. XPS study of MnO oxidation. *J. Electron Spectrosc. Relat. Phenom.* **1989**, *48*, 117–123.

(24) Allen, G.; Harris, S.; Jutson, J.; Dyke, J. A study of a number of mixed transition metal oxide spinels using X-ray photoelectron spectroscopy. *Appl. Surf. Sci.* **1989**, *37*, 111–134.

(25) Di Castro, V.; Polzonetti, G.; Contini, G.; Cozza, C.; Paponetti, B. XPS study of  $\text{MnO}_2$  minerals treated by bioleaching. *Surf. Interface Anal.* **1990**, *16*, 571–574.

(26) Goodenough, J. B.; Park, K. S. The Li-ion rechargeable battery: a perspective. *J. Am. Chem. Soc.* **2013**, *135*, 1167–1176.

(27) Dupin, J. C.; Gonbeau, D.; Vinatier, P.; Levasseur, A. Systematic XPS studies of metal oxides, hydroxides and peroxides. *Phys. Chem. Chem. Phys.* **2000**, *2*, 1319–1324.

(28) Sathiyaraj, M.; Rousse, G.; Ramesha, K.; Laisa, C. P.; Vezin, H.; Sougrati, M. T.; Doublet, M.-L.; Foix, D.; Gonbeau, D.; Walker, W.; Prakash, A. S.; Ben Hassine, M.; Dupont, L.; Tarascon, J.-M.; Prakash, A. S.; Ben Hassine, M.; Dupont, L.; Tarascon, J.-M. Reversible anionic redox chemistry in high-capacity layered-oxide electrodes. *Nat. Mater.* **2013**, *12*, 827–835.

(29) Qiao, R.; Wray, L. A.; Kim, J. H.; Pieczonka, N. P.; Harris, S. J.; Yang, W. Direct experimental probe of the Ni (II)/Ni (III)/Ni (IV) redox evolution in  $\text{LiNi}_{0.5}\text{Mn}_{1.5}\text{O}_4$  electrodes. *J. Phys. Chem. C* **2015**, *119*, 27228–27233.

(30) Hong, J.; Gent, W. E.; Xiao, P.; Lim, K.; Seo, D.-H.; Wu, J.; Csernica, P. M.; Takacs, C. J.; Nordlund, D.; Sun, C.-J.; Stone, K. H.; Passarello, D.; Yang, W.; Prendergast, D.; Ceder, G.; Toney, M. F.; Chueh, W. C. Metal–oxygen decoordination stabilizes anion redox in Li-rich oxides. *Nat. Mater.* **2019**, *18*, 256–265.

(31) Gent, W. E.; Lim, K.; Liang, Y.; Li, Q.; Barnes, T.; Ahn, S.-J.; Stone, K. H.; McIntire, M.; Hong, J.; Song, J. H.; Li, Y.; Mehta, A.; Ermon, S.; Tylliszczak, T.; Kilcoyne, D.; Vine, D.; Park, J.-H.; Doo, S.-K.; Toney, M. F.; Yang, W.; Prendergast, D.; Chueh, W. C. Coupling between oxygen redox and cation migration explains unusual electrochemistry in lithium-rich layered oxides. *Nat. Commun.* **2017**, *8*, 2091.

(32) Lee, G.-H.; Wu, J.; Kim, D.; Cho, K.; Cho, M.; Yang, W.; Kang, Y.-M. Reversible anionic redox activities in conventional  $\text{Li-Ni}_{1/3}\text{Co}_{1/3}\text{Mn}_{1/3}\text{O}_2$  cathodes. *Angew. Chem., Int. Ed.* **2020**, *59*, 8681.

(33) Roychoudhury, S.; Qiao, R.; Zhuo, Z.; Li, Q.; Lyu, Y.; Kim, J.-H.; Liu, J.; Lee, E.; Polzin, B. J.; Guo, J.; Yan, S.; Hu, Y.; Li, H.; Prendergast, D.; Yang, W. Deciphering the oxygen absorption pre-edge: a caveat on its application for probing oxygen redox reactions in batteries. *Energy Environ. Mater.* **2020**. DOI: 10.1002/eeem2.12119.

(34) Zhuo, Z.; Dai, K.; Qiao, R.; Wang, R.; Wu, J.; Liu, Y.; Peng, J.; Chen, L.; Chuang, Y.; Pan, F.; Shen, Z.; Liu, G.; Li, H.; Devereaux, T. P.; Yang, W. Cycling mechanism of  $\text{Li}_2\text{MnO}_3$ :  $\text{Li-CO}_2$  batteries and commonality on oxygen redox in cathode materials. *Joule* **2021**, *5*, 975–997.

(35) Shinshu, F.; Kaida, S.; Nagayama, M.; Nitta, Y. X-ray absorption fine structure study on Li-Mn-O compounds:  $\text{LiMn}_2\text{O}_4$ ,  $\text{Li}_4\text{Mn}_3\text{O}_{12}$  and  $\text{Li}_2\text{MnO}_3$ . *J. Power Sources* **1997**, *68*, 609–612.

(36) Ben, L.; Yu, H.; Chen, B.; Chen, Y.; Gong, Y.; Yang, X.; Gu, L.; Huang, X. Unusual spinel-to-layered transformation in  $\text{LiMn}_2\text{O}_4$  cathode explained by electrochemical and thermal stability investigation. *ACS Appl. Mater. Interfaces* **2017**, *9*, 35463–35475.

(37) Zhu, Z.; Wang, H.; Li, Y.; Gao, R.; Xiao, X.; Yu, Q.; Wang, C.; Waluyo, I.; Ding, J.; Hunt, A.; Li, J. A surface Se-substituted  $\text{LiCo}[\text{O}_{2-\delta}\text{Se}_\delta]$  cathode with ultrastable high-voltage cycling in pouch full-cells. *Adv. Mater.* **2020**, *32*, 2005182.

(38) Dong, Y.; Huang, Y.; Ding, D.; Wu, W.; Yao, X.; Li, J. Chemical and structural origin of hole states in yttria-stabilized zirconia. *Acta Mater.* **2021**, *203*, 116487.

(39) Seo, D. H.; Lee, J.; Urban, A.; Malik, R.; Kang, S.; Ceder, G. The structural and chemical origin of the oxygen redox activity in layered and cation-disordered Li-excess cathode materials. *Nat. Chem.* **2016**, *8*, 692.

(40) Yoon, M.; Dong, Y.; Hwang, J.; Sung, J.; Cha, H.; Ahn, K.; Huang, Y.; Kang, S. J.; Li, J.; Cho, J. Reactive boride infusion stabilizes Ni-rich cathodes for lithium-ion batteries. *Nat. Energy* **2021**, *6*, 362–371.

## Supplementary Information

### **Thermally Aged Li-Mn-O Cathode with Stabilized Hybrid Cation and Anion Redox**

Sa Li<sup>1,2\*</sup>, Xin Sun<sup>1,2</sup>, Yang Liu<sup>1,2</sup>, Guang Liu<sup>1,2</sup>, Weijiang Xue<sup>3</sup>, Iradwikanari Waluyo<sup>4</sup>, Zhi Zhu<sup>3</sup>, Yunguang Zhu<sup>5</sup>, Yanhao Dong<sup>3\*</sup>, Yunhui Huang<sup>1,2</sup>, and Ju Li<sup>3,6\*</sup>

<sup>1</sup>School of Materials Science and Engineering, Tongji University, Shanghai 201804, China

<sup>2</sup>Institute of New Energy for Vehicles, Tongji University, Shanghai 201804, China

<sup>3</sup>Department of Nuclear Science and Engineering, Massachusetts Institute of Technology, Cambridge, MA 02139, USA

<sup>4</sup>National Synchrotron Light Source II, Brookhaven National Laboratory, Upton, NY, USA

<sup>5</sup>Research Laboratory of Electronics, Massachusetts Institute of Technology, Cambridge, MA 02139, USA

<sup>6</sup>Department of Materials Science and Engineering, Massachusetts Institute of Technology, Cambridge, MA 02139, USA

## Experiment

**Synthesis of S-LMO.** We used a low-temperature solid-state synthesis method to prepare S-LMO. First,  $\text{MnCO}_3$  (Aladdin,99.95%) was mixed with  $\text{LiOH}\cdot\text{H}_2\text{O}$  (Adamas,99%). The molar ratio of Li and Mn was 4:5. After ground for 1 h, the obtained mixture was sintered at 400 °C for 12 h under air atmosphere to get the final material. Detailed characterizations of S-LMO can be found in Ref. 16.

**Synthesis of SL-LMO.** We used a 2<sup>nd</sup> step solid-state synthesis method to prepare SL-LMO. First,  $\text{MnCO}_3$  (Aladdin,99.95%) was mixed with  $\text{LiOH}\cdot\text{H}_2\text{O}$  (Adamas,99%). The molar ratio of Li and Mn was 4:5. After ground for 1 h, the obtained mixture was sintered at 400 °C for 12 h under air atmosphere and then heated to 600 °C and kept for 2 h to get the final material.

**Material characterizations.** X-ray diffraction was performed on Rigaku Ultima IV. It was operated in the  $2\theta$  value range of 10° to 80° with a 2°/min scanning rate. The morphology of the SL-LMO sample was identified by Quanta 200 field emission scanning electron microscope (FESEM). The HRTEM images were taken on a transmission electron microscope JEM-2100F with accelerating voltage of 200 kV. X-ray photoelectron spectroscopy (XPS) measurement was carried out by use of ESCALAB 250Xi.

**Electrochemical tests.** CR2025-type coin cells, assembled in a glove box filled with dry argon gas, were used for electrochemical tests. A coin cell consisted of a cathode electrode, an anode, ceramic membrane and organic electrolyte. To fabricate the cathode electrode, active materials and carbon black were mixed with polyvinylidene fluoride (PVDF) binder (8:1:1, weight ratio) in appropriate amount of N-methylpyrrolidone (NMP), using magnetic stirring to mix fully. The obtained slurry was cast onto an aluminum foil current collector. Then, it was dried at 80 °C overnight in a vacuum oven. The organic electrolyte was 1 mol/L  $\text{LiPF}_6$  in a mixture of equal volumes of ethylene carbonate (EC) and dimethyl carbonate (DMC). For half cells and full cells, the anodes were lithium metal,  $\text{Li}_4\text{Ti}_5\text{O}_{12}$  and lithium-tin alloy respectively. The electrochemical tests were carried out on a battery test system (Neware). Electrochemical impedance spectroscopy (EIS) data was performed on a CHI600A Electrochemical workstation (Chinster, Shanghai, China), with 5 mV ac excitation over a frequency range of 1 mHz to 100 kHz. Cyclic voltammogram (CV) test was performed at a scan rate of 0.2 mV/s among voltage range of 1.8 V to 4.7 V (vs.  $\text{Li}^+/\text{Li}$ ) by a CHI600A Electrochemical workstation (Chinster, Shanghai, China). Rate performances of S-LMO and SL-LMO were tested on a battery test system (Neware) at 0.1 C up to 4 C (1 C defined as 200 mA/g). DEMS analysis was used to detect and analyze the gas during cycling, and DEMS analyses of the SL-LMO and S-LMO

cathodes in half cells were tested with a constant current density of 0.32 mA/cm<sup>2</sup> with the loading of 16 mg/cm<sup>2</sup> when charging to 4.7 V in the first cycle.

**High-temperature in situ XRD.** X-ray diffraction pattern of S-LMO was measured in the  $2\theta$  range of 15° to 70° with a 5°/min scanning rate at 400 °C and 500 °C, and during 2 h holding at 600 °C.

**Soft X-ray absorption spectroscopy (sXAS) measurements.** Soft X-ray absorption spectroscopy (sXAS) measurements of O K edge in partial fluorescence yield (PFY) mode from 520 to 565 eV were carried out at the IOS (23-ID-2) beamline of National Synchrotron Light Source II at Brookhaven National Laboratory. We followed the same normalization methodology as in the literature.<sup>1,2</sup> For each sample, the PFY-sXAS were collected from four local areas and the average intensity is firstly normalized by an individual photodiode scan. A linear sloping background is next removed by linear fitting of the flat low-temperature region from 520.0 to 523.0 eV before the absorption peaks. Lastly, then spectrum is normalized by setting the low-energy region to zero intensity and the main peak to unity intensity.

## Simulations

Vienna *ab initio* simulation package (VASP) was used to conduct spin-polarized first-principles calculations by projector augmented-wave (PAW) method with Perdew-Burke-Ernzerhof (PBE) generalized gradient approximation (GGA).<sup>3-5</sup> PAW potentials with  $2s^1$  electron for Li,  $3d^54s^2$  electrons for Mn, and  $2s^22p^4$  electrons for O were used. DFT+*U* calculations were performed with  $U=3.9$  eV and  $J=0$  eV for Mn  $3d$  orbitals.<sup>6,7</sup> We used a plane-wave cutoff energy of 520 eV, set the convergence criterion to have residue atomic forces of  $<0.05$  eV/Å, and sampled the Brillouin zone using Monkhorst-Pack scheme with a  $3\times3\times3$  **k**-point mesh. To simulate spinel Li<sub>4</sub>Mn<sub>5</sub>O<sub>12</sub>, we used a supercell containing 16 Li, 20 Mn, and 48 O, and Li/Mn disorder was simulated by a random distribution of the 4 Li and 20 Mn on the octahedral site. To simulate delithiated spinel Li<sub>3.5</sub>Mn<sub>5</sub>O<sub>12</sub> and Li<sub>3</sub>Mn<sub>5</sub>O<sub>12</sub>, 2 or 4 randomly chosen Li were removed from the Li<sub>4</sub>Mn<sub>5</sub>O<sub>12</sub> supercell with random octahedral Li/Mn distribution. The schematic atomic structures were plotted using VESTA.<sup>8</sup>

## References

1. Luo, K.; Roberts, M. R.; Hao, R.; Guerrini, N.; Pickup, D. M.; Liu, Y. S.; Edström, K.; Guo, J.; Chadwick, A. V.; Duda, L. C. Charge-compensation in 3 d-transition-metal-oxide intercalation cathodes through the generation of localized electron holes on oxygen. *Nat. Chem.* **2016**, *8*, 684.
2. Luo, K.; Roberts, M. R.; Guerrini, N.; Tapia-Ruiz, N.; Hao, R.; Massel, F.; Pickup, D. M.; Ramos, S.; Liu, Y. S.; Guo, J. Anion redox chemistry in the cobalt free 3d transition metal oxide intercalation electrode Li [Li<sub>0.2</sub>Ni<sub>0.2</sub>Mn<sub>0.6</sub>] O<sub>2</sub>. *J. Am. Chem. Soc.* **2016**, *138*, 11211-11218.
3. Kresse, G.; Joubert, D. From ultrasoft pseudopotentials to the projector augmented-wave method. *Phys. Rev. B* **1999**, *59*, 1758.

4. Kresse, G.; Furthmüller, J. Efficient iterative schemes for ab initio total-energy calculations using a plane-wave basis set. *Phys. Rev. B* **1996**, *54*, 11169.
5. Perdew, J. P.; Burke, K.; Ernzerhof, M. Generalized gradient approximation made simple. *Phys. Rev. Lett.* **1996**, *77*, 3865.
6. Dudarev, S.; Botton, G.; Savrasov, S.; Humphreys, C.; Sutton, A. Electron-energy-loss spectra and the structural stability of nickel oxide: an LSDA+ U study. *Phys. Rev. B* **1998**, *57*, 1505.
7. Jain, A.; Hautier, G.; Ong, S. P.; Moore, C. J.; Fischer, C. C.; Persson, K.; Ceder, G. Formation enthalpies by mixing GGA and GGA+ U calculations. *Phys. Rev. B* **2011**, *84*, 045115.
8. Momma, K.; Izumi, F. VESTA 3 for three-dimensional visualization of crystal, volumetric and morphology data. *J. Appl Crystallogr.* **2011**, *44*, 1272-1276.

**Table S1 Density and porosity of cathode samples (four samples are tested)**

Sample	Loading (mg/cm <sup>2</sup> )	Cathode thickness (μm)	Electrode density (g/cm <sup>3</sup> )	Compact density (g/cm <sup>3</sup> )
1	28.62	106	2.7	2.8
2	30.24	112	2.7	2.8
3	29.97	111	2.7	2.8
4	29.16	108	2.7	2.8

Here the weight ratio of active material: binder: conductive carbon = 92:4:4. The density of binder is 1.8 g/cm<sup>3</sup> and the density of conductive carbon is 0.26 g/cm<sup>3</sup>.

**Table S2 Related standard PDF cards of  $\text{Li}_4\text{Mn}_5\text{O}_{12}$ ,  $\text{Li}_2\text{MnO}_3$  and  $\text{LiMn}_2\text{O}_4$** 

$\text{Li}_4\text{Mn}_5\text{O}_{12}$			$\text{Li}_2\text{MnO}_3$			$\text{LiMn}_2\text{O}_4$		
2 Theta	d (nm)	(hkl)	2 Theta	d (nm)	(hkl)	2 Theta	d (nm)	(hkl)
18.817	0.471	(111)	20.082	0.426	(020)	18.611	0.476	(111)
36.483	0.246	(311)	/	/	/	36.085	0.249	(311)
58.734	0.157	(511)	/	/	/	58.056	0.158	(511)

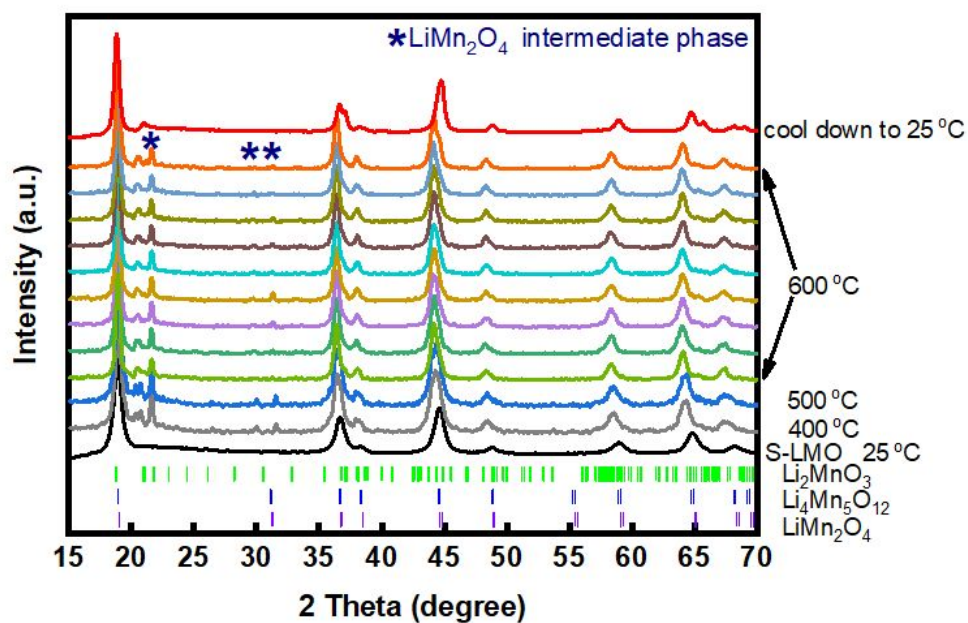


**Figure S1** High-temperature in situ XRD of S-LMO upon heating and room-temperature ex situ XRD of S-LMO and SL-LMO.

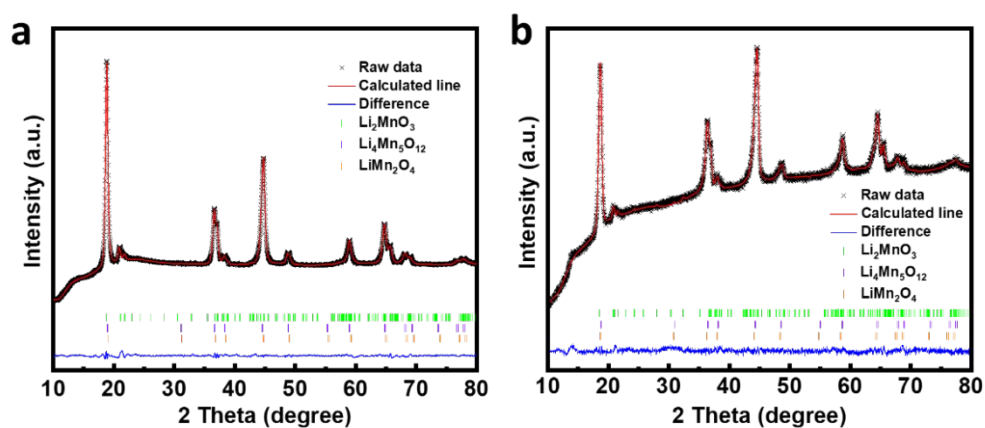


**Figure S2** XRD refinements of SL-LMO of: (a) the pristine state and (b) after cycling state.

According to the XRD refinement of the pristine state, the mass ratios of  $\text{Li}_4\text{Mn}_5\text{O}_{12}$ ,  $\text{LiMn}_2\text{O}_4$  and  $\text{Li}_2\text{MnO}_3$  are 49%, 36% and 15%, respectively. According to the XRD refinement of SL-LMO after cycling state, the mass ratios of  $\text{Li}_4\text{Mn}_5\text{O}_{12}$ ,  $\text{LiMn}_2\text{O}_4$  and  $\text{Li}_2\text{MnO}_3$  are 52%, 37% and 11%, respectively.

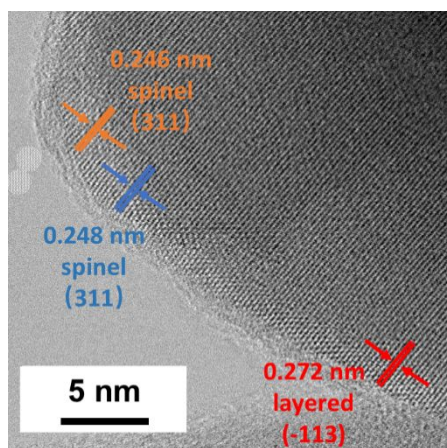


**Figure S3** HRTEM images of SL-LMO cathode at the near-surface region.

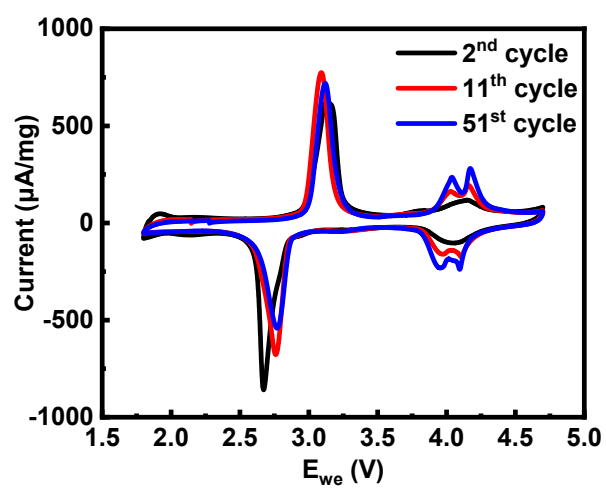


**Figure S4** CV curves of SL-LMO cathode in the 2<sup>nd</sup>, 11<sup>th</sup>, 51<sup>st</sup> cycle, conducted at 0.2 mV/s to track the voltage evolution upon cycling.

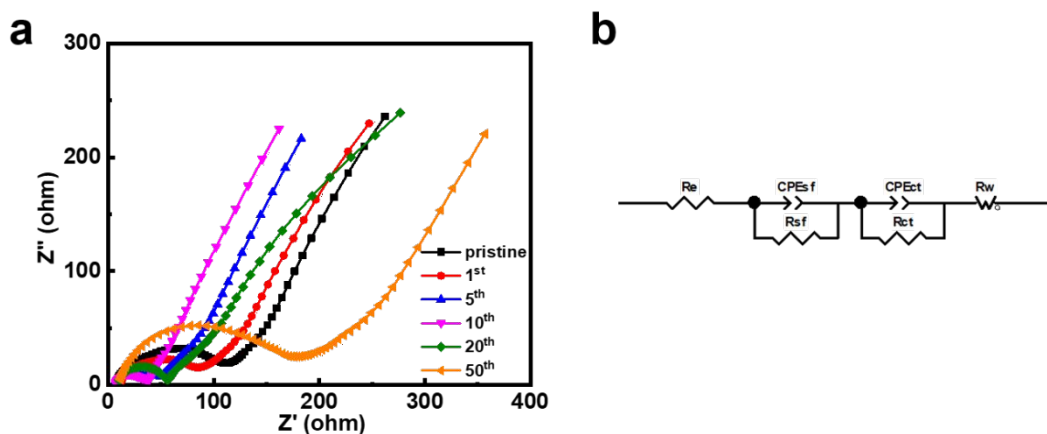


**Figure S5** (a) EIS of SL-LMO cathode before cycle and after 1<sup>st</sup>, 5<sup>th</sup>, 10<sup>th</sup>, 20<sup>th</sup>, 50<sup>th</sup> cycle at a discharge state of 1.8 V, (b) the equivalent circuit model to simulate the cell.

It is tested at room temperature before cycling, after the initial cycle, and after 5, 10, 20, 50 cycles, respectively. The Nyquist plots of cells are illustrated in Figure S5a and the equivalent-circuit model is illustrated in Figure S5b. We can see that the charge-transfer resistance value before cycling is 120.4  $\Omega$ , and yet the value after 10 cycles is only 38.2  $\Omega$ . Smaller charge-transfer resistance after 10 cycles is mainly attributed to the activation of the initial inactive  $Li_2MnO_3$  phase, and it corroborates with the increase of capacities during the starting cycles. And the charge-transfer resistance value increases to 52  $\Omega$  after 20 cycles and 153  $\Omega$  after 50 cycles, respectively, which causes the resistance-induced capacity to drop during cycles. But the resistances of cathode before cycle and after 50 cycles are still low, which corresponds to the considerably good rate performance of SL-LMO cathode. Since the generation of gas would usually cause bubbles in the system, which cuts down the  $Li^+$  transportation pathway, leading to higher internal resistance, the gradual decrement of impedance in the first 10 cycles also suggests the successful suppression of  $O_2$  release due to the immunization.

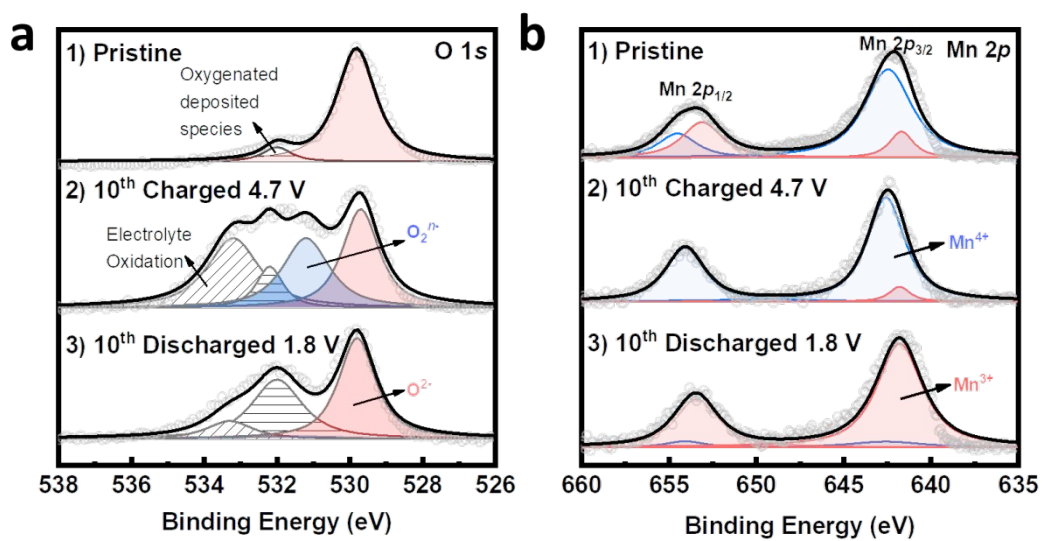


**Figure S6** XPS at various states of electrochemical cycling after etching 50 nm of the surface. (a) O 1s XPS spectra, (b) Mn 2p XPS spectra.

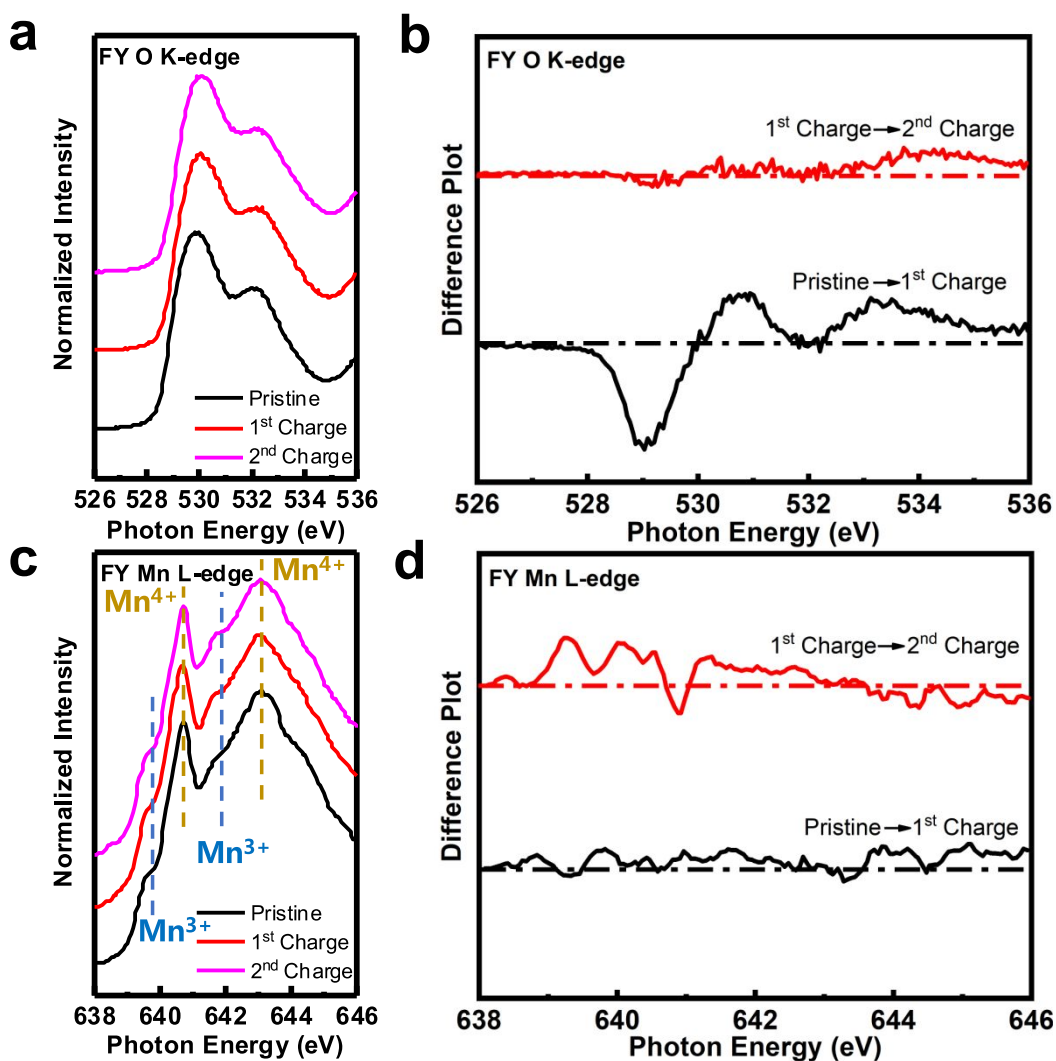


**Figure S7** (a) PFY-sXAS of O K-edges of SL-LMO cathode of the pristine state, after 1<sup>st</sup> charge to 4.7 V and after 2<sup>nd</sup> charge to 4.7 V, and the curves are normalized by setting the low-energy region at 526.0 eV to zero intensity and the main peak region at ~530.0 eV to unity intensity; (b) Difference plot of sXAS obtaining from (a) showing the intensity evolution of O-K XAS pre-edge; (c) PFY-sXAS of Mn L-edges of SL-LMO cathode of the pristine state, after 1<sup>st</sup> charge to 4.7 V and after 2<sup>nd</sup> charge to 4.7 V, and the curves are normalized by setting the low-energy region at 638.0 eV to zero intensity and the main peak region at ~643.0 eV to unity intensity. Mn<sup>3+</sup> and Mn<sup>4+</sup> are referred to *Nat. Energy* **2019**, *4*, 1049-1058, and a small amount of Mn<sup>3+</sup> is detected in the three curves, which should come from the surface signal of the nanoparticles; (d) Difference plot of sXAS obtaining from (c) showing the intensity evolution of Mn L-edges.

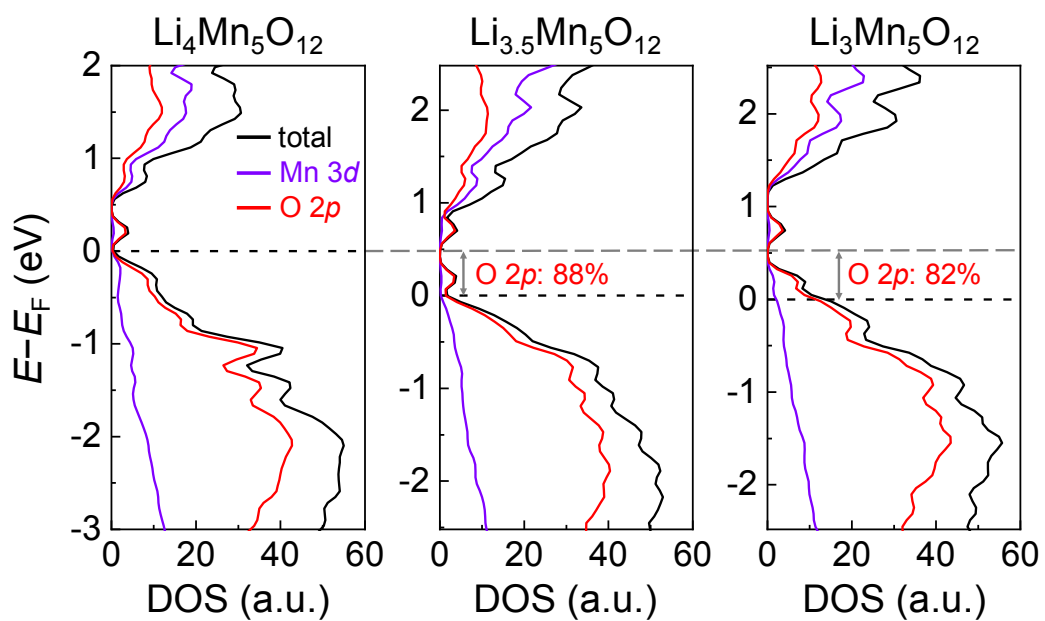


**Figure S8.** Calculated partial densities of states of O  $2p$  and Mn  $3d$  states in  $\text{Li}_4\text{Mn}_5\text{O}_{12}$ ,  $\text{Li}_{3.5}\text{Mn}_5\text{O}_{12}$ , and  $\text{Li}_3\text{Mn}_5\text{O}_{12}$ , all with random octahedral Li/Mn distribution.

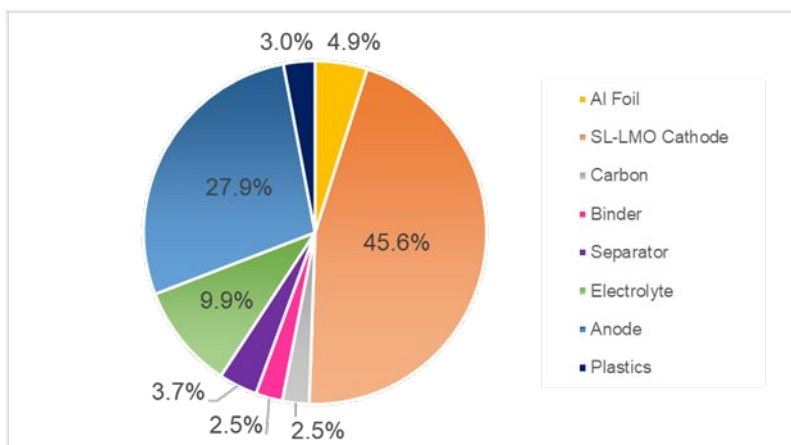


**Figure S9** Battery configuration of SL-LMO//Li<sub>x</sub>Sn full cell in terms of weight percentage.

We considered the composite cathode consisted of 90 wt% SL-LMO, 5 wt% binder and 5 wt% conductive carbon, and the full pouch cell was with 0.5× lithium excess. The full-cell energy is estimated to be 316 Wh/kg, and energy density of the total battery achieves 307 Wh/kg.

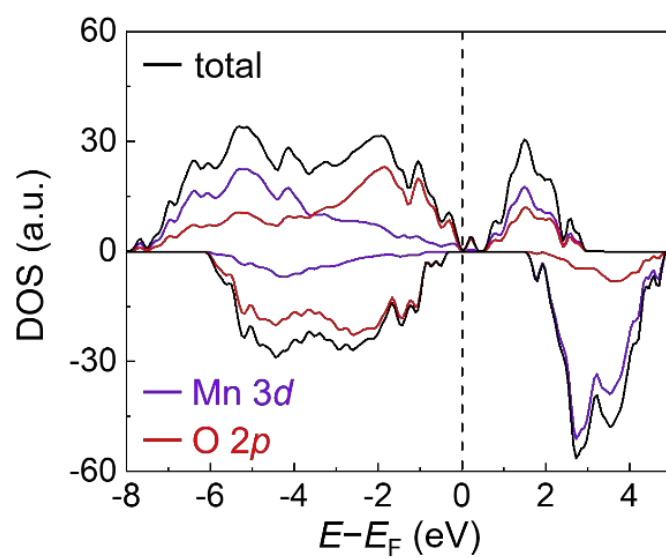


**Figure S10** Calculated total density of states (DOS) and DOS of Mn 3*d* and O 2*p* states for octahedral-Li/Mn-disordered  $\text{Li}_4\text{Mn}_5\text{O}_{12}$ . The positive and negative values for DOS represent positive and negative spin states, respectively.